ARTICLES
https://doi.org/10.1038/s41563-020-0794-5

nature materials

Atomic-resolution electron microscopy of nanoscale local structure in lead-based relaxor ferroelectrics

Abinash Kumar[1], Jonathon N. Baker[2], Preston C. Bowes[2], Matthew J. Cabral[2], Shujun Zhang[3], Elizabeth C. Dickey[2], Douglas L. Irving[2] and James M. LeBeau[1]✉

Relaxor ferroelectrics, which can exhibit exceptional electromechanical coupling, are some of the most important functional materials, with applications ranging from ultrasound imaging to actuators. Since their discovery, their complex nanoscale chemical and structural heterogeneity has made the origins of their electromechanical properties extremely difficult to understand. Here, we employ aberration-corrected scanning transmission electron microscopy to quantify various types of nanoscale heterogeneities and their connection to local polarization in the prototypical relaxor ferroelectric system $Pb(Mg_{1/3}Nb_{2/3})O_3$–$PbTiO_3$. We identify three main contributions that each depend on Ti content: chemical order, oxygen octahedral tilt and oxygen octahedral distortion. These heterogeneities are found to be spatially correlated with low-angle polar domain walls, indicating their role in disrupting long-range polarization and leading to nanoscale domain formation and the relaxor response. We further locate nanoscale regions of monoclinic-like distortion that correlate directly with Ti content and electromechanical performance. Through this approach, the connections between chemical heterogeneity, structural heterogeneity and local polarization are revealed, validating models that are needed to develop the next generation of relaxor ferroelectrics.

Relaxor ferroelectrics are distinguished from traditional ferroelectrics by their frequency dependent, diffuse phase transitions that are commonly attributed to the existence of nanoscale order[1]. Among this class of materials, Pb-based systems remain essential as they exhibit the largest known piezoelectric coefficients and outstanding dielectric properties[2–4]. These properties have been commonly attributed to the existence of polar nanoregions in the material that align to the applied field[5,6]. This simple model fails, however, to explain relaxor behaviour in a variety of materials, including polymer-based systems[7]. The recently proposed 'polar slush' model overcomes these limitations by considering a multi-domain polar state with low-energy, low-angle domain walls formed throughout[8]. Model validation has, however, been hindered by the seemingly endless number of structural characterization studies with differing interpretations, leading these systems to be described as a 'hopeless mess'[1].

$Pb(Mg_{1/3}Nb_{2/3})O_3$–$PbTiO_3$ (PMN-PT) is the prototypical Pb-based relaxor ferroelectric system and exhibits state-of-the-art properties. For example, piezoelectric constants up to 4,100 $pC\,N^{-1}$ have been achieved via Sm doping[9]. PMN-PT adopts the perovskite structure (formula ABO_3) with the A sublattice occupied by Pb and the B sublattice occupied by either Mg, Nb or Ti. Furthermore as $PbTiO_3$ is added to PMN, the system reaches a morphotropic phase boundary (MPB) with x in the range 30–32%, where the electromechanical properties are maximized[10]. Deciphering the origins of these enhanced properties is, however, complicated by the nanoscale heterogeneity of chemistry and structure. While X-ray and neutron scattering are the main characterization methods used to explain these details, making direct connections between composition, structure and polarization has proved exceedingly difficult[11–17]. For example, while nanoscale chemical ordering of the B sublattice cations was one of the first signatures revealed[17,18] and is found to varying degrees in all Pb-based relaxor ferroelectrics[19,20], its details are still being explored[21–23].

Capturing a complete picture of the connection between chemistry, structure and polarization in relaxor ferroelectrics requires characterization techniques that are able to account for both cation and anion sublattices. While distortions of the oxygen sublattice have been previously detected[24], a combination of X-ray and neutron diffraction recently discovered that correlated oxygen displacements are likely integral to bringing forth the outstanding electromechanical properties in PMN-PT (ref. [10]). Diffraction characterization methods, however, lack the spatial resolution required to directly determine the origin of nanoscale polar variation[25,26]. By contrast, annular dark-field scanning transmission electron microscopy (ADF STEM), Fig. 1a, can readily image the projected crystal structure at the atomic length scale and is sensitive to chemical distribution[21]. Unfortunately, ADF images are dominated by cation contrast that precludes detailed detection and quantification of light elements such as oxygen. Recently, annular bright-field (ABF)[27,28] and integrated differential phase contrast (iDPC)[29,30] STEM techniques have been developed to overcome these challenges. While iDPC can detect the cation and oxygen atom column positions, as shown in Fig. 1a, it too has a major drawback: the image contrast lacks the atomic number interpretability of ADF STEM. On the other hand, both limitations can be overcome by simultaneously capturing ADF and iDPC images, with the resulting datasets akin to merging results from X-ray and neutron diffraction techniques, and enabling correlation between polarization, chemistry and structure directly at the atomic scale.

[1]Department of Materials Science and Engineering, Massachusetts Institute of Technology, Cambridge, MA, USA. [2]Department of Materials Science and Engineering, North Carolina State University, Raleigh, NC, USA. [3]Institute for Superconducting and Electronic Materials, Australian Institute of Innovative Materials, University of Wollongong, Wollongong, New South Wales, Australia. ✉e-mail: lebeau@mit.edu

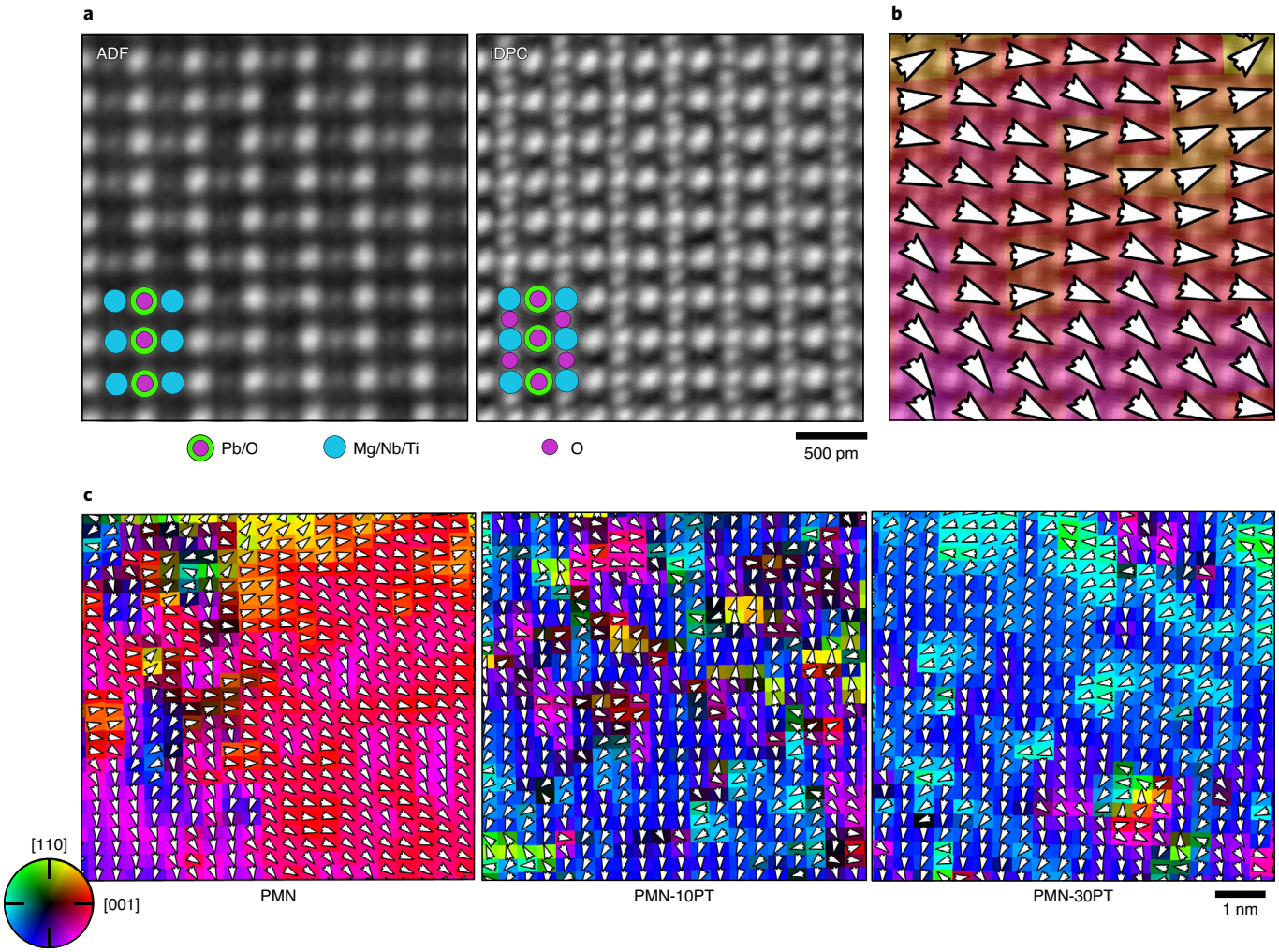

Fig. 1 | Atomic resolution polarization mapping. a,**b**, Simultaneously acquired ADF and iDPC images of PMN along the <1$\bar{1}$0> projection (**a**) with the projected displacement (polarization) map from iDPC (**b**). **c**, Projected displacement (polarization) for PMN-*x*PT (*x*=0, 10 and 30) unit cells in representative iDPC images. The projected displacement (polarization) magnitude ranges from 1 to 20pm and is indicated by luminosity.

Here, we investigate the structural and chemical origins of relaxor ferroelectric properties in PMN-*x*PT ($x=0$, 10 and 30). Through a combination of ADF and iDPC aberration-corrected STEM, the projected positions of cation and anion sublattices are used to measure the subtle features of nanoscale polarization in these materials. The projected polarization reveals the presence of nanoscale domains that are consistent with the polar slush model[8]. We further quantify the distribution of chemical and structural heterogeneities as a function of Ti content, and a direct correlation is found between the spatial distribution of chemical/structural heterogeneities and polarization domain walls. The heterogeneities are found to inhibit polarization rotation, leading to the formation of low-angle domain walls. In combination, these results provide evidence for the underlying mechanisms responsible for yielding relaxor behaviour.

Mapping nanoscale polarization variation. Using iDPC STEM, the projected polarization is measured across ten different sample locations using the approach outlined in the Methods; the influence of projection on these measurements is explored in Supplementary Information Section 1. These datasets yield approximately 5,000 analysed unit cells at each of the three PMN-PT compositions. The high sampling of each composition provides a statistical representation of the underlying structure of the material, aiding in connecting the results presented here to prior diffraction studies. Calculating the centre of mass difference between the cations and anions using iDPC STEM, Fig. 1c shows representative projected polarization maps for PMN, PMN-10PT and PMN-30PT imaged along <1$\bar{1}$0>. The projected polarization exhibits regions with similar magnitude and direction—that is, polar domains—that vary smoothly across each image.

Notably for PMN, the observed polar domains do not decay to a non-polar background, which contrasts with the polar nanoregion model that assumes a non-polar matrix. These nanoscale domains vary in size from 2 to 12 nm and form low-angle domain walls between them, which are located using the method described in Supplementary Information Section 2. This observation is also remarkably similar to reverse Monte Carlo analysis of diffraction data[23]. Moreover, a substantial majority (72%) of the domain wall angles are in the range 10–35°, which agrees with predictions from the polar slush model (see Supplementary Information Section 2)[8,31]. As the fraction of PT increases, the average domain wall angle increases, reflecting the onset of ferroelectric behaviour. This behaviour leads to the mixed relaxor and ferroelectric properties found in PMN-PT materials and expected from the polar slush model[8,31]. This model does not, however, incorporate the specific structure and chemistry details that drive the formation of the polar domains.

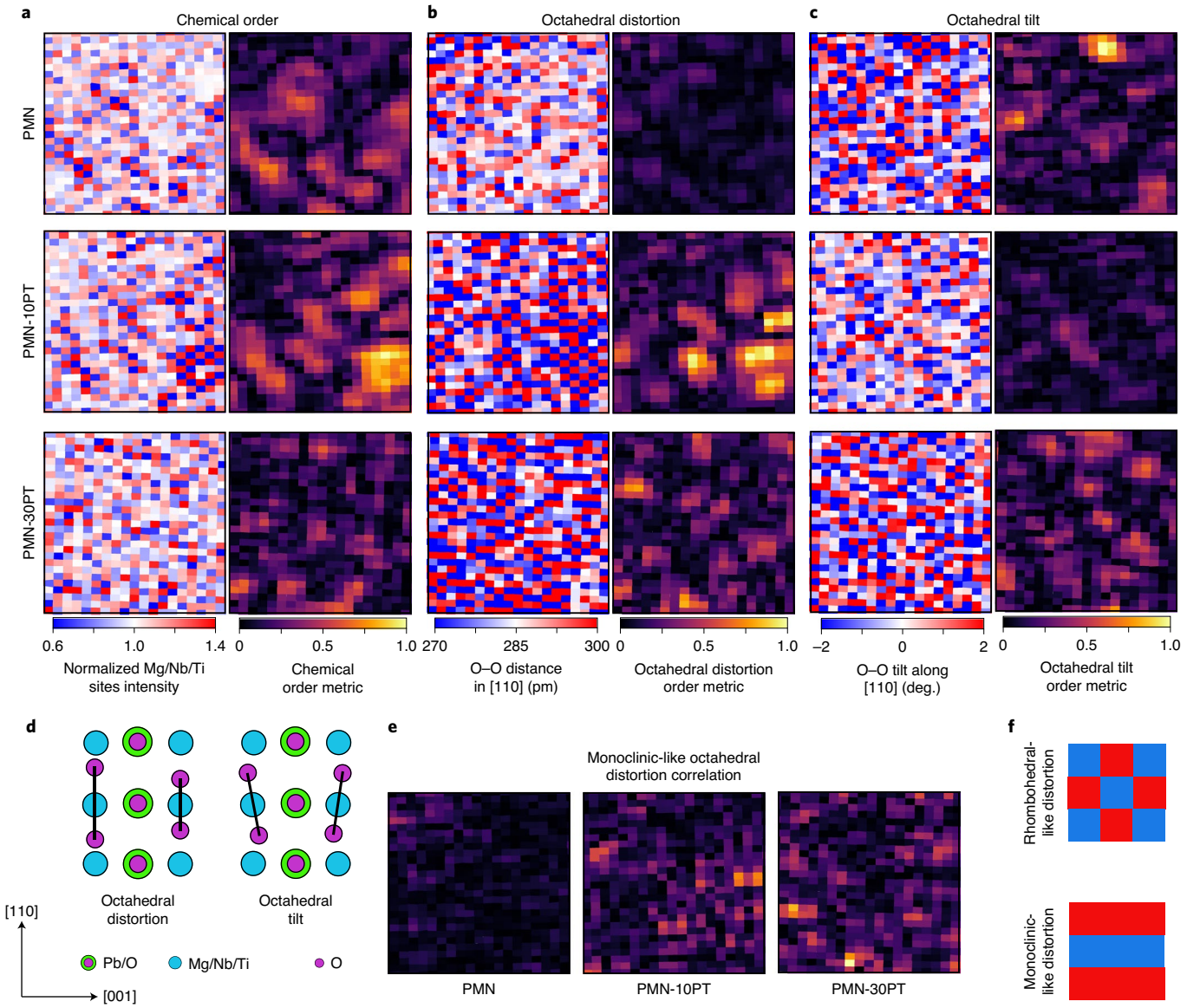

Fig. 2 | Distribution of structural and chemical heterogeneities. a, Chemical order. **b**, Octahedral distortion. **c**, Octahedral tilt. **d**, Schematic of distortion types and their corresponding O–O patterns. **e**, Monoclinic-like distortion analysis. **f**, Schematic patterns of rhombohedral-like and monoclinic-like distortion.

Quantifying the types of local order. Chemical ordering is revealed in the ADF STEM data, as shown in Fig. 2a, left. Clustered oscillation of B sublattice atom column intensity on (111) planes indicates a doubled perovskite lattice where occupancy of Mg and Nb vary systematically. The weaker normalized intensity atom columns (blue) contain more Mg or Ti (denoted β_I), while those stronger intensity atom columns (red) contain more Nb (denoted β_{II}). Correlation analysis, shown in Fig. 2a and detailed in Supplementary Information Section 3, is used to quantify the relative fraction of these chemically ordered regions (CORs). At each composition, the CORs are found throughout and account for $39 \pm 1\%$ of the total projected area in the case of PMN, $37 \pm 2\%$ for 10% PT and only $11 \pm 1\%$ for 30% PT. The decreasing chemical order with increasing Ti agrees with previous X-ray, electron, and neutron scattering results where superlattice reflection intensity also decreases as the composition approaches the MPB[10,32].

Recently, Krogstad suggested the presence of anti-ferrodistortive displacements based on diffuse scattering features; that is, Pb displaces in the opposite direction of its B sublattice neighbours[10]. The chemical and spatial origins of this behaviour could not, however, be unambiguously determined. Based on the iDPC STEM data, and extensively in the CORs, the Pb atom columns are anti-ferrodistortive relative to the B sites (Supplementary Information Section 4). These anti-ferrodistortive displacements decrease in accordance with the decreasing COR density as PT content increases, in agreement with Krogstad.

As noted from recent X-ray and neutron scattering experiments, oxygen displacements may hold the key to understanding structure–property relationships in Pb-based relaxors[10]. To this end, oxygen octahedral distortion (expansion/compression) and tilting (schematically shown in Fig. 2d) are determined from iDPC images, as in Fig. 2b,c. At each composition, distortion and tilting exhibit local ordering, reminiscent of the CORs.

Similar correlation analysis (see Supplementary Information Section 3) is used to determine the area fraction of octahedral distortion regions (ODRs), as shown in Fig. 2b. In PMN, 21% of the

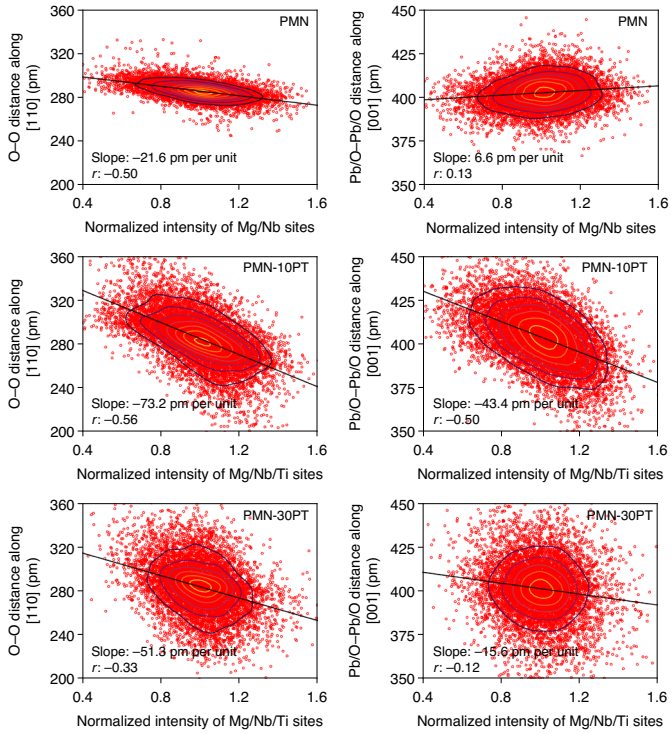

Fig. 3 | Correlation between atom column chemistry and the local distortion. Measurements of the Mg/Nb/Ti normalized atom column intensity and the O–O distance along [110] or Pb/O–Pb/O distance along [001], as indicated. *r* is Pearson's correlation coefficient.

projected area exhibits distortion ordering, with 63% overlapping the CORs and 27% at the COR boundaries. The overlap of the CORs and ODRs highlights the spatial correlation between octahedral distortion and chemical ordering. As PT content increases, the ODRs increase to 28% for PMN-10PT. Furthermore, a similar chequerboard octahedral distortion pattern is predicted for the chemically ordered PMN from density functional theory (DFT; Supplementary Information Sections 5 and 6).

With PMN-30PT, however, the distortion order changes. Rather than exhibiting the rhombohedral-like, chequerboard distortion pattern (see Fig. 2f), the distortion becomes predominately striped on (110) planes, which indicates the formation of monoclinic-like unit cells as verified with STEM image simulations (Supplementary Fig. 11) and agrees with prior diffraction studies[11]. The area fractions of rhombohedral- and monoclinic-like distortions were determined by use of the correlation analysis approach discussed in Supplementary Information Section 3. As Ti content increases, so too does monoclinic-like distortion, as shown in Fig. 2e. Moreover, this type of local planar distortion should give rise to asymmetric diffuse scattering[33]. Importantly, Krogstad[10] found that the oxygen-mediated asymmetric diffuse scattering in neutron scattering was the only feature linked to the piezoelectric properties. The results presented here confirm that oxygen displacements are key and that they originate in monoclinic-like regions. It is also important to note that due to the presence of gradients in local chemistry and structure, pure phases (rhombohedral or monoclinic) are not observed. From this, one can argue that such strong local structural variations and short correlation lengths give rise to local triclinic symmetry, which can facilitate the free rotation of polarization by small angles. This finding further supports the polar slush model's description of relaxors.

Beyond expansion and contraction, the oxygen octahedra also tilt with respect to [110], as shown in Fig. 2c. Applying correlation analysis (see Supplementary Information Section 3), 19% of the total projected area exhibits octahedral tilt ordering in PMN. Analysis of the B sublattice atom column intensities in and around these octahedral tilt regions (OTRs) shows that the atom column intensities are normally distributed (see Supplementary Information Section 7). Thus the OTRs do not occur at the interior of the CORs but form in close proximity to the boundary between CORs. Furthermore, these regions are rich in magnesium, as exhibited by the shift in mean column intensities towards lower values (Supplementary Fig. 13). Taken together with the DFT-determined bond length distributions, these findings suggest a mechanism for the OTRs. Specifically, Mg–O bond lengths are much more strongly conserved than Nb–O bond lengths. As a result, Mg–O–Mg bonded octahedra would be more likely to tilt rather than stretch. Moreover, because Mg–O–Mg bonds can only exist in regions that are not chemically ordered (Supplementary Fig. 7), such tilting is expected to be especially pronounced in transition regions due to the change in local chemistry.

The anti-phase tilt pattern suggests the presence of local rhombohedral, *R*3*c*, symmetry[34]. With increasing PT, the OTR area decreases from 11% to 5% for 10PT and 30PT, respectively. As the fraction of these features decreases with composition, their disappearance also explains another distinct diffuse scattering contribution noted by Krogstad that had both temperature-dependent and -independent components. While the temperature-independent contribution is thought to originate from the CORs, the temperature-dependent part arises from the octahedral tilt ordering that is disrupted by thermal fluctuations. The intensity of this type of diffuse scattering is found to decrease with PT content and follows the same trend as OTRs quantified from STEM.

Relating local chemistry and structure. Combining the ADF and iDPC STEM data, the change in B-site chemistry measured with the Mg/Nb/Ti atom column intensity is found to correlate to the O–O neighbour distance, as shown in Fig. 3. In each case, the B sublattice intensity is negatively correlated with the O–O atom column distances[35]. This shows that Mg/Ti expands the local oxygen sublattice, while Nb leads to contraction, which is consistent with the prior reports[23,36,37]. In combination with the response of oxygen at the MPB where the O–O spread increases, the observed correlation indicates the key role of Ti to disrupt the lattice to stabilize the monoclinic-like distortion and increase the piezoelectric coefficient. The Pb/O–Pb/O atom column distances, in comparison, show weak to no correlation with variation in B-site chemistry in PMN as shown in Fig. 3, likely due to the dominant contribution of Pb on the observed atom column positions (Supplementary Information Section 1).

PMN-10PT, by contrast, exhibits moderate, negative correlation as shown in Fig. 3. For PMN-30PT, substantially larger distortions are observed that correspond to the increased polarization and piezoelectric coefficient. This correlated structural variation in Pb displacement also explains the diffuse scattering feature found by Krogstad that correlates to the cation size mismatch. Furthermore, the above-mentioned correlation is important, as nearly ~10,000 atom columns are used in the analysis.

Further analysis of the PMN-10PT β_{I} and β_{II} normalized intensities (Supplementary Fig. 12) also reveals that their intensity difference is enhanced with the introduction of Ti. This suggests that Ti initially replaces Nb in the mixed β_{I} sites of the CORs, leading to a concomitant decrease in intensity for those atom columns and increased image contrast. Importantly, the preferential incorporation of Ti to the CORs can be explained by analysis of the B sublattice bond lengths from DFT, albeit via an indirect argument. Any covalent bond has an ideal length or range of lengths it prefers to adopt for any particular coordination environment, and adopting bond lengths outside of this range is associated with severe energetic

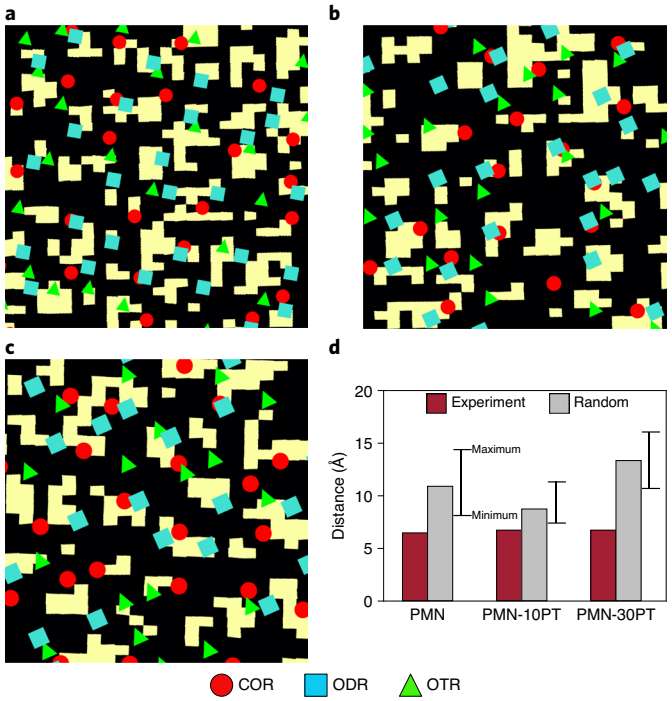

Fig. 4 | Spatial relationship between domain walls and inhomogeneities. **a**–**c**, Positions of COR, ODR, OTR maxima and domain walls for PMN (**a**), PMN-10PT (**b**) and PMN-30PT (**c**). Domain walls occur at the blocked, yellow regions. **d**, The distance at which 95% of the heterogeneities are within that distance to a nearest domain wall, from experiment and the average of randomly generated datasets. The error bars represent the minimum and maximum 95% distances that were measured across all randomly generated datasets for each composition.

penalties and a commensurate decrease in the likelihood of incorporation. For example, in oxide perovskites, titanium tends to prefer bond lengths between 1.9 and 2.2 Å (refs. [38–41]). Supplementary Fig. 8 shows the ratio of B sites in the simulated COR and disordered structures with bond lengths within a certain range. It is clear from this figure that, for a given bond length window, the COR structure has substantially more sites close to Ti's ideal octahedral bonding environment than the disordered structure, especially when considering five and six B–O bonds. In fact, the COR structure has between two and three times more sites available than the disordered structure over most of the bond length range considered, and nearly 20 times more in the most extreme case. These high ratios result from the 2–4 pm differences in the onset of optimal coordination environments between the two systems, and indicate that Ti can form more strong bonds in the chemically ordered regions than in the disordered regions without changing any other bond lengths or otherwise altering the structures. All else being equal, this strongly suggests that Ti will preferentially incorporate into the CORs, at least on the PMN side of the composition space where CORs form.

Linking polarization and heterogeneity. The heterogeneity distribution is also found to link directly with the local variation in polarization and domain walls. First, the centres of the CORs, ODRs and OTRs are identified as maxima in the results from correlation analysis as detailed in Supplementary Information Section 8. Qualitatively, in Fig. 4a–c, the heterogeneity maxima occur at, or very near, the locations of greatest polarization variation, that is, low-angle domain walls.

The observed relationship between ordered heterogeneities and domain walls is validated by quantifying the nearest neighbour distance. As shown in Fig. 4d, 95% of the heterogeneities are within a distance of 1.5 to 2 unit cells of the nearest domain wall regardless of PT content. Across the composition range investigated, 1/3 of CORs, 1/3 of ODRs and 1/3 of OTRs are within this distance of the domain walls. In addition, 1/3 of the domain walls have at least two nearby types of structural or chemical ordering. This indicates that the polar domain walls cannot be explained by a single type of heterogeneity, but require the consideration of all features identified.

To determine the importance of this observation, consider the null hypothesis that heterogeneities are randomly distributed with respect to polarization. Taking 10,000 random sets of data equivalent to experiment, but with random heterogeneity locations, the 95% threshold is not reached until a distance two times larger than experiment; see Fig. 4d. Further highlighting the difference, the error bars indicate the maximum and minimum 95% distances for the 10,000 datasets at each composition. A result similar to experiment is not found in any of the random data, indicating that P is significantly less than 0.05, safely discounting the null hypothesis. Taken together, the results presented here unambiguously reveal that chemical and structural heterogeneities are not randomly distributed with respect to polarization, but instead act as the mechanism to disrupt the formation of long-range polarization. Although this role of heterogeneity has been postulated[17,42], we are able to directly observe the disruptive effects.

Outlook. The combination of nanoscale features explains the origin for relaxor ferroelectric behaviour in PMN-PT that leads to the dramatically improved piezoelectric performance. Thus, to design materials with higher piezoelectric coefficients, balancing order (chemical and/or octahedral distortion/tilt) with disorder is key. In other words, to support relaxor behaviour, barriers to polarization rotation need to be distributed throughout the material at a concentration that disrupts long-range (ferroelectric) polarization. For example, this tuning might be achieved by changing the alloy composition, adding dopants or modifying synthesis conditions. Broadly, engineering a combination of short-range structural and chemical order will be essential for advancing the next generation of Pb-free relaxor ferroelectric materials.

Online content

Any methods, additional references, Nature Research reporting summaries, source data, extended data, supplementary information, acknowledgements, peer review information; details of author contributions and competing interests; and statements of data and code availability are available at https://doi.org/10.1038/s41563-020-0794-5.

Received: 20 November 2019; Accepted: 4 August 2020;
Published online: 7 September 2020

References

1. Cohen, R. E. Relaxors go critical. *Nature* **441**, 941–942 (2006).
2. Park, S.-E. & Shrout, T. R. Ultrahigh strain and piezoelectric behavior in relaxor based ferroelectric single crystals. *J. Appl. Phys.* **82**, 1804 (1997).
3. Zhang, S. & Li, F. High performance ferroelectric relaxor-$PbTiO_3$ single crystals: Status and perspective. *J. Appl. Phys.* **111**, 031301 (2012).
4. Zhang, S. et al. Advantages and challenges of relaxor-$PbTiO_3$ ferroelectric crystals for electroacoustic transducers—a review. *Prog. Mater. Sci.* **68**, 1–66 (2015).
5. Burns, G. & Dacol, F. H. Glassy polarization behavior in ferroelectric compounds $Pb(Mg_{1/3}Nb_{2/3})O_3$ and $Pb(Zn_{1/3}Nb_{2/3})O_3$. *Solid State Commun.* **48**, 853–856 (1983).
6. Burns, G. & Dacol, F. H. Crystalline ferroelectrics with glassy polarization behavior. *Phys. Rev. B* **28**, 2527–2530 (1983).
7. Yang, L. et al. Relaxor ferroelectric behavior from strong physical pinning in a poly(vinylidene fluoride-co-trifluoroethylene-co-chlorotrifluoroethylene) random terpolymer. *Macromolecules* **47**, 8119–8125 (2014).

8. Takenaka, H., Grinberg, I., Liu, S. & Rappe, A. M. Slush-like polar structures in single-crystal relaxors. *Nature* **546**, 391–395 (2017).
9. Li, F. et al. Giant piezoelectricity of Sm-doped $Pb(Mg_{1/3}Nb_{2/3})O_3$-$PbTiO_3$ single crystals. *Science* **364**, 264–268 (2019).
10. Krogstad, M. J. et al. The relation of local order to material properties in relaxor ferroelectrics. *Nat. Mater.* **17**, 718–724 (2018).
11. Singh, A. K., Pandey, D. & Zaharko, O. Powder neutron diffraction study of phase transitions in and a phase diagram of $(1-x)$ $[Pb(Mg_{1/3}Nb_{2/3})O_3]$ -$x$$PbTiO_3$. *Phys. Rev. B* **74**, 024101 (2006).
12. Singh, A. K. & Pandey, D. Evidence for M_B and M_C phases in the morphotropic phase boundary region of $(1-x)$ $[Pb(Mg_{1/3}Nb_{2/3})O_3]$ $-x$$PbTiO_3$: a Rietveld study. *Phys. Rev. B* **67**, 064102 (2003).
13. Thomas, N. W., Ivanov, S. A., Ananta, S., Tellgren, R. & Rundlof, H. New evidence for rhombohedral symmetry in the relaxor ferroelectric $Pb(Mg_{1/3}Nb_{2/3})O_3$. *J. Eur. Ceram. Soc.* **19**, 2667–2675 (1999).
14. Kim, K. H., Payne, D. A. & Zuo, J. M. Symmetry of piezoelectric $(1-x)$ $Pb(Mg_{1/3}Nb_{2/3})O_3$-$x$$PbTiO_3$ ($x=0.31$) single crystal at different length scales in the morphotropic phase boundary region. *Phys. Rev. B* **86**, 184113 (2012).
15. Cowley, R. A., Gvasaliya, S. N., Lushnikov, S. G., Roessli, B. & Rotaru, G. M. Relaxing with relaxors: a review of relaxor ferroelectrics. *Adv. Phys.* **60**, 229–327 (2011).
16. Davis, M. Picturing the elephant: giant piezoelectric activity and the monoclinic phases of relaxor-ferroelectric single crystals. *J. Electroceramics* **19**, 25–47 (2007).
17. Randall, C. A. & Bhalla, A. S. Nanostructural-property relations in complex lead perovskites. *Jpn. J. Appl. Phys.* **29**, 327–333 (1990).
18. Randall, C. A., Bhalla, A. S., Shrout, T. R. & Cross, L. E. Classification and consequences of complex lead perovskite ferroelectrics with regard to B-site cation order. *J. Mater. Res.* **5**, 829–834 (1990).
19. Takesue, N. et al. Effects of B-site ordering/disordering in lead scandium niobate. *J. Phys. Condens. Matter* **11**, 8301–8312 (1999).
20. Goossens, D. J. Local ordering in lead-based relaxor ferroelectrics. *Acc. Chem. Res.* **46**, 2597–2606 (2013).
21. Cabral, M. J., Zhang, S., Dickey, E. C. & LeBeau, J. M. Gradient chemical order in the relaxor $Pb(Mg_{1/3}Nb_{2/3})O_3$. *Appl. Phys. Lett.* **112**, 082901 (2018).
22. Kopecký, M., Kub, J., Fábry, J. & Hlinka, J. Nanometer-range atomic order directly recovered from resonant diffuse scattering. *Phys. Rev. B* **93**, 054202 (2016).
23. Eremenko, M. et al. Local atomic order and hierarchical polar nanoregions in a classical relaxor ferroelectric. *Nat. Commun.* **10**, 2728 (2019).
24. Rosenfeld, H. D. & Egami, T. Short and intermediate range structural and chemical order in the relaxor ferroelectric lead magnesium niobate. *Ferroelectrics* **164**, 133–141 (1995).
25. Keen, D. A. & Goodwin, A. L. The crystallography of correlated disorder. *Nature* **521**, 303–309 (2015).
26. Xu, G., Wen, J., Stock, C. & Gehring, P. M. Phase instability induced by polar nanoregions in a relaxor ferroelectric system. *Nat. Mater.* **7**, 562–566 (2008).
27. Findlay, S. D. et al. Robust atomic resolution imaging of light elements using scanning transmission electron microscopy. *Appl. Phys. Lett.* **95**, 191913 (2009).
28. Kim, Y. M., Pennycook, S. J. & Borisevich, A. Y. Quantitative comparison of bright field and annular bright field imaging modes for characterization of oxygen octahedral tilts. *Ultramicroscopy* **181**, 1–7 (2017).
29. Lazić, I., Bosch, E. G. & Lazar, S. Phase contrast STEM for thin samples: integrated differential phase contrast. *Ultramicroscopy* **160**, 265–280 (2016).
30. de Graaf, S., Momand, J., Mitterbauer, C., Lazar, S. & Kooi, B. J. Resolving hydrogen atoms at metal-metal hydride interfaces. *Sci. Adv.* **6**, eaay4312 (2020).
31. Kim, J. et al. Epitaxial strain control of relaxor ferroelectric phase evolution. *Adv. Mater.* **31**, 1901060 (2019).
32. Hilton, A. D., Barber, D. J., Randall, C. A. & Shrout, T. R. On short range ordering in the perovskite lead magnesium niobate. *J. Mater. Sci.* **25**, 3461–3466 (1990).
33. Kreisel, J. et al. High-pressure X-ray scattering of oxides with a nanoscale local structure: application to $Na_{1/2}Bi_{1/2}TiO_3$. *Phys. Rev. B* **68**, 014113 (2003).
34. Glazer, A. M. The classification of tilted octahedra in perovskites. *Acta Crystallogr. B* **28**, 3384–3392 (1972).
35. Sang, X., Grimley, E. D., Niu, C., Irving, D. L. & LeBeau, J. M. Direct observation of charge mediated lattice distortions in complex oxide solid solutions. *Appl. Phys. Lett.* **106**, 061913 (2015).
36. Kvyatkovskii, O. E. Oxygen position in $Pb(Mg_{1/3}Nb_{2/3})O_3$ from *ab initio* cluster calculations. *Ferroelectrics* **299**, 55–57 (2004).
37. Sepliarsky, M. & Cohen, R. E. First-principles based atomistic modeling of phase stability in PMN–xPT. *J. Phys. Condens. Matter* **23**, 435902 (2011).
38. Abramov, Y. A., Tsirelson, V., Zavodnik, V., Ivanov, S. & Brown, I. The chemical bond and atomic displacements in $SrTiO_3$ from X-ray diffraction analysis. *Acta Crystallogr. B* **51**, 942–951 (1995).
39. Cole, S. S. & Espenschied, H. Lead titanate: crystal structure, temperature of formation, and specific gravity data. *J. Phys. Chem.* **41**, 445–451 (1937).
40. Shin, Y.-H., Son, J.-Y., Lee, B.-J., Grinberg, I. & Rappe, A. M. Order-disorder character of $PbTiO_3$. *J. Phys. Condens. Matter* **20**, 015224 (2008).
41. Yoshiasa, A. et al. High-temperature single-crystal X-ray diffraction study of tetragonal and cubic perovskite-type $PbTiO_3$ phases. *Acta Crystallogr. B* **72**, 381–388 (2016).
42. Fu, D. et al. Relaxor $Pb(Mg_{1/3}Nb_{2/3})O_3$: a ferroelectric with multiple inhomogeneities. *Phys. Rev. Lett.* **103**, 207601 (2009).

Methods

Sample information. PMN-*x*PT single crystals were grown via the high-temperature flux method. Samples for electron microscopy were cut from these larger single crystals and oriented along $<1\bar{1}0>$ and then thinned to electron transparency using mechanical wedge polishing[43] followed by low-temperature, low-energy Ar ion milling.

STEM. STEM imaging was performed with a probe-corrected FEI Titan G2 60–300 kV electron microscope equipped with an extreme field emission gun (X-FEG) at a beam current of 30 pA and probe convergence semi-angle of 19.6 mrad. We used a custom scripting interface to automate the Thermo Fisher Scientific Velox software for simultaneous ADF and iDPC acquisition. ADF images were collected with a collection semi-angle range of 34–205 mrad and iDPC with a collection semi-angle range of 7–28 mrad. For high image accuracy and precision, the revolving STEM method was used[44,45]. Each revolving STEM dataset consisted of 20 1,024 × 1,024 pixel frames with a 90° rotation between each successive frame. Sample thickness ranged from 6 to 10 nm as determined using position-averaged convergent beam electron diffraction[46]. Because polarization is linearly proportional to the net displacement of cations from anions in a unit cell[47], the projected polarization is calculated from iDPC images as the difference between the cation and anion centres of mass. Atom column centres are extracted from drift and scan distortion-corrected iDPC images using a custom Python-based atom column indexing method[48].

DFT and image simulations. DFT calculations of PMN were performed to investigate the atomic structures in three dimensions, and to examine charge localization and bond length distributions. These calculations were performed with the Perdew–Burke–Ernzerhof (PBE) exchange correlation functional in the Vienna Ab initio Simulation Package (VASP) 5.3.3, collinear spin polarization and a plane wave kinetic energy cut-off of 520 eV (refs. [49–52]). A single reciprocal space point at Γ was used. Projector augmented wave pseudopotentials were used with 2, 11, 4 and 6 valence electrons explicitly treated for Mg, Nb, Pb and O, respectively. Additional details of the calculation are provided in Supplementary Information Section 5.

For STEM image simulations, supercells were constructed using relaxed structures from DFT. A repeating unit was cropped and simulated using a custom Python-based STEM image simulation software. Simulated ADF and iDPC images were convolved with a Gaussian with full-width at half-maximum of 80 pm to approximately account for the finite effective source size[53].

Data availability

The image datasets analysed during the current study are available from https://doi.org/10.7910/DVN/F0FHTG. Other data is available from the corresponding author by reasonable request. Source data are provided with this paper.

Code availability

Custom Python scripts used to analyse STEM images are available from the corresponding author upon request.

References

43. Voyles, P. M., Muller, D. A., Grazul, J. L., Citrin, P. H. & Gossmann, H.-J. L. Atomic-scale imaging of individual dopant atoms and clusters in highly *n*-type bulk Si. *Nature* **416**, 826–829 (2002).
44. Sang, X. & LeBeau, J. M. Revolving scanning transmission electron microscopy: correcting sample drift distortion without prior knowledge. *Ultramicroscopy* **138**, 28–35 (2014).
45. Dycus, J. H. et al. Accurate nanoscale crystallography in real-space using scanning transmission electron microscopy. *Microsc. Microanal.* **21**, 946–952 (2015).
46. LeBeau, J. M., Findlay, S. D., Allen, L. J. & Stemmer, S. Position averaged convergent beam electron diffraction: theory and applications. *Ultramicroscopy* **110**, 118–125 (2010).
47. Tao, H. et al. Ultrahigh performance in lead-free piezoceramics utilizing a relaxor slush polar state with multiphase coexistence. *J. Am. Chem. Soc.* **141**, 13987–13994 (2019).
48. Sang, X., Oni, A. A. & LeBeau, J. M. Atom column indexing: atomic resolution image analysis through a matrix representation. *Microsc. Microanal.* **20**, 1764–1771 (2014).
49. Kresse, G. & Hafner, J. *Ab initio* molecular dynamics of liquid metals. *Phys. Rev. B* **47**, 558–561 (1993).
50. Kresse, G. & Hafner, J. *Ab initio* molecular-dynamics simulation of the liquid-metal–amorphous-semiconductor transition in germanium. *Phys. Rev. B* **49**, 14251–14269 (1994).
51. Kresse, G. & Furthmüller, J. Efficiency of ab-initio total energy calculations for metals and semiconductors using a plane-wave basis set. *Comput. Mater. Sci.* **6**, 15–50 (1996).
52. Kresse, G. & Furthmüller, J. Efficient iterative schemes for *ab initio* total-energy calculations using a plane-wave basis set. *Phys. Rev. B* **54**, 11169–11186 (1996).
53. LeBeau, J. M., Findlay, S. D., Allen, L. J. & Stemmer, S. Quantitative atomic resolution scanning transmission electron microscopy. *Phys. Rev. Lett.* **100**, 206101 (2008).

Acknowledgements

We thank the National Science Foundation for support for this work, as part of the Center for Dielectrics and Piezoelectrics under grant nos IIP-1841453 and IIP-1841466. S.Z. acknowledges support from the Australian Research Council (FT140100698) and the Office of Naval Research Global (N62909-18-12168). P.C.B. was supported by the Department of Defense through the National Defense Science and Engineering Graduate (NDSEG) fellowship programme. Computational time and financial support for J.N.B. was provided by AFOSR grant FA9550-17-1-0318. M.J.C. acknowledges support from the National Science Foundation as part of the NRT-SEAS under grant no. DGE-1633587. This work was performed in part at the Analytical Instrumentation Facility (AIF) at North Carolina State University, which is supported by the State of North Carolina and the National Science Foundation (ECCS-1542015). AIF is a member of the North Carolina Research Triangle Nanotechnology Network (RTNN), a site in the National Nanotechnology Coordinated Infrastructure (NNCI). The NVIDIA Titan Xp GPU used for this research was donated by the NVIDIA Corporation. We thank M. Hauwiller for useful suggestions while preparing the manuscript.

Author contributions

A.K. conducted the electron microscopy experiments, data analysis and image simulations. M.J.C. prepared the PMN samples for electron microscopy and collected STEM data. S.Z. grew the PMN-*x*PT single crystals. J.N.B., P.C.B. and D.L.I. performed the DFT calculations and the corresponding analysis. J.M.L. and E.C.D. designed the electron microscopy experiments and guided the research. All authors co-wrote and edited the manuscript.

Competing interests

The authors declare no competing interests.

Additional information

Supplementary information is available for this paper at https://doi.org/10.1038/s41563-020-0794-5.

Correspondence and requests for materials should be addressed to J.M.L.

Reprints and permissions information is available at www.nature.com/reprints.